AIAA SciTech Forum
23-27 January 2023, National Harbor, MD & Online
AIAA SCITECH 2023 Forum
10.2514/6.2023-0353

On the effect of high-frequency plasma actuator forcing for prevention of dynamic stall

Alexander James Lilley* and Subrata Roy†
Applied Physics Research Group at the University of Florida, Gainesville, FL, 32611

Miguel R. Visbal‡
Air Force Research Laboratory, Wright-Patterson AFB, Ohio 45433, USA

The influence of a linear plasma actuator on dynamic stall is studied for a sinusoidally pitching NACA0012 airfoil. The Reynolds number for the incoming flow is $\mathrm{Re}_c = 2 \times 10^5$. The phenomenon is observed experimentally using Particle Image Velocimetry. The plasma actuator generates forcing that is partially normal and tangential to the leading edge. The plasma actuator frequencies of $\mathrm{St}_f = 10$, $\mathrm{St}_f = 26.6$, and $\mathrm{St}_f = 50$ are considered in comparison to actuator off performance. Next, counter-flow and co-flow plasma actuator orientations are compared. The airfoil pitches sinusoidal between $\alpha = 4°$ and $\alpha = 18°$ with a reduced frequency of $k = \pi/16$. A gradient of flow control effectiveness was observed with increasing Strouhal number (St_f). The high-frequency case ($\mathrm{St}_f = 50$) prevented dynamic stall for the entire motion observed. When comparing counter-flow and co-flow, the counter-flow was more effective in delaying dynamic stall showing that the delay is due to the high frequency forcing and not momentum addition.

I. Nomenclature

c	=	chord length, [m]
f	=	actuation frequency, [Hz]
k	=	reduced frequency, $\frac{1}{2}\omega \times c/U_\infty$
kV_{pp}	=	kiloVolts peak to peak, [kV]
Re_c	=	chord length scaled Reynolds number, $\rho U_\infty c/\mu$
St_f	=	Strouhal number based on actuation frequency, fc/U_∞
t	=	time, [s]
$t*$	=	non-dimensional time, tU_∞/c
U_∞	=	freestream velocity, [m/s]
α	=	angle of attack, [deg]
μ	=	dynamic viscosity, $[N/(m^2 s)]$
ω	=	angular frequency, [rad/s]
Ω_+	=	non-dimensional angular frequency, $\omega c/U_\infty$
$\lvert\omega_z\rvert$	=	Vorticity magnitude in the z-direction, $\lvert\frac{\partial v}{\partial x} - \frac{\partial u}{\partial y}\rvert$

II. Introduction

The delay of dynamic stall is highly desirable for rotorcrafts, fixed wing aircrafts, and micro air vehicles. The defining features of deep dynamic stall are a temporary increase in lift followed by an abrupt loss of lift when the dynamic stall vortex separates. This abrupt loss of lift is preceded by a change in pitching moment from up to down.

From an aircraft perspective, the airfoil can undergo structural damages from vibration due to twisting and bending forces induced by the occurrence of dynamic stall. Aerostructural interactions can lead to a positive feedback loop compounding damage. Besides structural preservation, delay of dynamic stall is desirable as a method to increase

*Research Assistant, PhD candidate at the University of Florida
†Professor, Mechanical and Aerospace Department Associate Fellow
‡Computational Fluid Dynamics Technical Advisor, Aerodynamic Technology Branch, AFRL/RQVA. Fellow AIAA

aircraft performance. In the case of fighter jets performing high alpha maneuvers, higher angles of attack can be achieved were dynamic stall to be delayed. For a rotorcraft in forward motion, the top speed is limited by the retreating blade dynamic stall.

Extensive research has been performed on dynamic stall delay over the past decades including experimental and numerical work [1][2][3]. Bulk flow techniques include slats [4] and vortex generators[5]. Carr and McAlister found leading edge slats to maintain lift coefficient and reduce negative pitch moment through a motion up to $\alpha = 25$[4]. Despite successes, slats have slow response time and require heavy mechanisms to implement. Another bulk flow approach, Vortex generators can delay dynamic stall, although vortex generators increase drag. Heine et al. found success using vortex generators to increase lift coefficient during upstroke and significant increase during down-stroke. Bulk flow techniques have shown promise but may be impractical for some real world applications such as helicopter blades, which may be too thin to implement slats and which may be too drag sensitive to implement vortex generators.

A practical control solution which has few implementation draw backs are plasma actuators. Plasma actuators are simple devices composed of an exposed electrode which is surface mounted, a dielectric, and an electrode that is embedded in the dielectric. High alternating voltage is applied across the electrodes causing plasma to form. The plasma imparts a net momentum, which can be used for flow control or thrust. Plasma actuators have significantly less raw control authority than standard flow control methods such as flaps. Plasma actuators' strength lies in their light weight and high-frequency response. To implement plasma actuators only 2 thin electrodes, an amplifier and a power source are necessary. Aircraft already have electrical systems which can be leveraged as power sources, especially considering use cases for plasma actuators are short term and intermittent. The frequency response of plasma actuators is significantly higher than turbine bleed or flaps. Plasma actuators can operate on frequencies of the order of 10^4 and previous research has shown their ability to operate in wet conditions [6].

Post and Corke explored dynamic stall delay using plasma actuators for a NACA0015 at $\mathrm{Re}_c = 76,000$ pitching at a reduced frequency, k= 0.08 with a sinusoidal motion of $\alpha = 15^\circ + 10^\circ sin(\omega t)$ [7]. An increase in lift was found when when considering a triangle wave with frequency of $5kHz$ as the carrier signal and the $20Hz$ as the message signal[7]. Post and Corke then note that when considering the pitch moment curve in conjunction with the lift curve, the case with the unsteady $80Hz$ message signal was most desirable[7]. Similar work was performed by Lombardi et al. where a NACA0015 was pitched at the reduced frequency, k, of 0.08 with a free stream velocity of 10 m/s[8]. A plasma actuator with a carrier signal of $3.5kHz$ and messenger signal of $80Hz$ was selectively used via a controller to delay dynamic stall [8].

Diverging from the idea that $\mathrm{St}_f = 1$ would be the most effective forcing, Visbal explored high-frequency ($\mathrm{St}_f = 50$) surface normal 3D zero net mass forcing[9]. Numerical simulations were performed for a NACA0012 at $\mathrm{Re} = 5 \times 10^5$ for a constant non-dimensional pitch rate of $\Omega_+ = 0.05$ starting at $\alpha_0 = 4^\circ$. Visbal found a delay in leading edge suction collapse of approximately 7.3° from $\alpha = 14.7^\circ$ to $\alpha = 22^\circ$. Lilley et al. experimentally investigated sinusoidal forcing at $\mathrm{St}_f = 50$ for a NACA0012 pitching at $\Omega_+ = 0.050$[10]. Using flow visualizations, Lilley et al. estimated a delay in dynamic stall of 3° [10].

In the present work we consider control without amplitude modulation which is typically used in SDBD based approaches for delaying dynamic stall [7][8][11][12]. The effect of actuator on and off, effect of frequency, and effect of actuator orientation are explored. The frequencies considered are $\mathrm{St}_f = 10$, $\mathrm{St}_f = 26.6$, and $\mathrm{St}_f = 50$. The orientation of the actuator considered are counter-flow and co-flow. The airfoil undergoes sinusoidal motion between 4° and 18° angle of attack with a reduced frequency of $k = \pi/16$. The Reynolds number is $\mathrm{Re}_c = 2.0 \times 10^5$.

III. Experimental Procedure

All experiments in this paper are done using the Applied Physics Research Group (APRG) Wind Tunnel at the University of Florida. The wind tunnel uses 4 meshes, $915mm$ length settling chamber, and contraction ratio of 8.11 : 1 to condition the flow. The test cross section is $210mm \times 210mm$ and the length is $610mm$. The airfoil is a NACA0012 and its angle of attack is positioned using a NEMA34. Thick acrylic disks placed on either side of the wing enforce wall boundary conditions and finite span. The plasma actuator exposed electrode is on the suction side leading edge of the wing and the embedded is biased towards the pressure side of the leading edge. The Reynolds number is $\mathrm{Re}_c = 2.0 \times 10^5$. Details of the model design, experimental setup and diagnostics are described in the following subsections.

A. Model Design

In order to reduce flow interference, the wing is designed such that all fasteners, except two, are embedded. Fixed wall conditions are implemented using 4 mm acrylic disks to prevent 3D interactions associated with the gap between the wind tunnel wall and model[13] (see Fig. 1).

The airfoil is 3D printed using a Photon Mono X (Masked Stereo Lithography). The resin Siraya Blu is used for its high structural integrity. The airfoil is sanded from 400 grit to 3000 grit to ensure the smoothest possible surface. The airfoil uses a slot which is integral to its structure to mate with a steel shaft that is mounted to the wind tunnel wall. The steel shaft mounted to the wind tunnel wall is driven by a NEMA34 stepper motor.

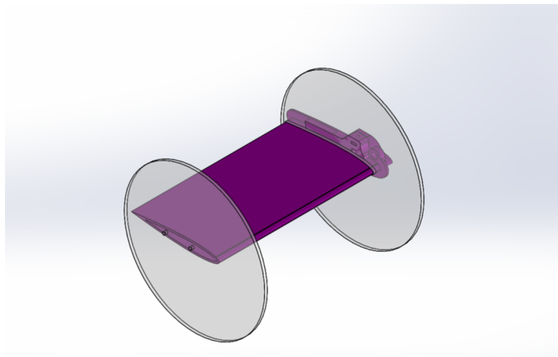

Fig. 1 Isometric view of the airfoil model used. Two transparent discs are used to implement the fixed wall condition. From Lilley et al. [10]

The airfoil has a chord length of 10 cm and a span of 17.5 cm. The plasma actuator used on this airfoil is a linear actuator with straight edge. The exposed electrode is on the suction side of the airfoil, while the embedded electrode is within the airfoil biased towards the pressure side. The high voltage AC and ground wires are embedded within the airfoil. The exposed electrode has a span of 16 cm while the grounded electrode spans 17.5 cm. The edges of the exposed electrode are insulated using Kapton tape to prevent arcing.

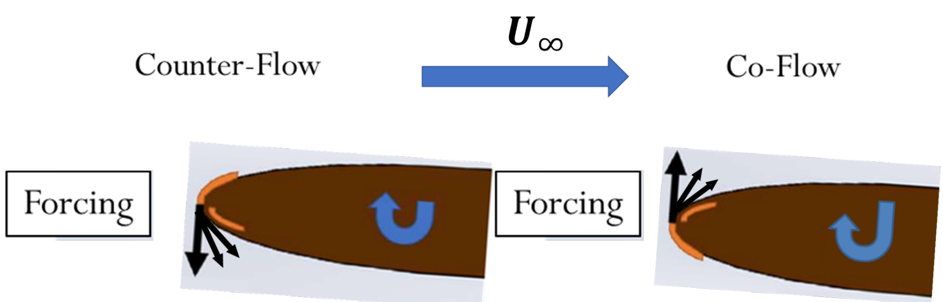

Fig. 2 Schematics of the counter and co-flow actuator orientations. Image modified from Lilley et al. [10]

The actuator is placed contouring around the leading edge of the NACA0012 airfoil. The exposed electrode is $25mm$wide beginning at the leading edge. The embedded electrode is $3.125mm$ wide and is held via an insert near the leading edge (Fig 2). There are two possible orientations of the linear plasma actuator, co-flow and counter-flow (see Fig. 2). In the co-flow orientation, the plasma force is aligned to the freestream flow while in the counter-flow orientation plasma forcing is opposing the flow.

In order to obtain the high voltage AC signal at the exposed electrode, a Tektronix arbitrary function generator (Model AFG3022B), a QSC 1850 HD RMX audio amplifier, and a custom Corona Magnetics transformer are used. The voltage applied at the exposed electrode is 16.5 kilo-Volts peak-to-peak (kVpp). The frequencies of the signals considered are: 3000 Hz, 8000 Hz, and 15,000 Hz, which correspond to St_f = 10, 26.6, and 50, respectively. A schematic from Lilley et al[10] can be seen in Fig. 3.

B. Particle Image Velocimetry (PIV)

Since the wind tunnel is an open loop construction adjacent to the room being considered office space, the PIV seed must be safe and carefully controlled. The seed is generated using a 400 Watt thermal fogging machine. The mixture

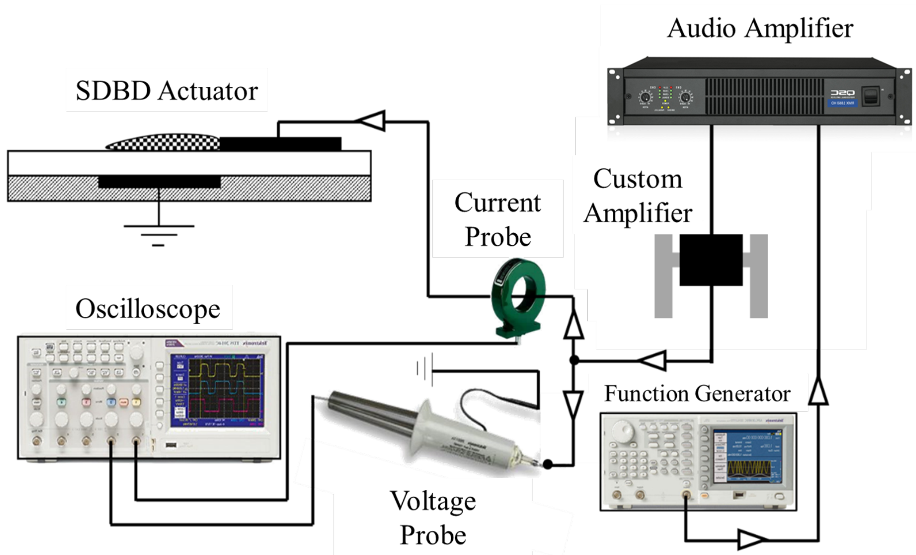

Fig. 3 Electronic setup for powering the plasma actuator. Image and caption from Lilley et al. [10]

used is a 3:2 distilled water to glycerine mixture. The seed is mixed with air using an impeller that helps homogeneous mixing of the seed. The glycerine-water mixture is introduced at the entrance of the tunnel via a bendable plastic hose and a thin elongated diffuser. A CCD Imager Pro X Camera with a 2048 × 2048 resolution is used to record two images that correspond to a single PIV frame. To illuminate the seed, a single laser pulse from a 523nm New Wave Research 14 Hz Nd:YAG is used. The camera has an exposure time of 5μs.

To avoid laser reflections, for purposes of preserving the camera and observing near-wall effects, Rhodamine 6G paint is used in conjunction with optical camera filters. The Rhodamine 6G paint fluoresces 532nm primarily in the 590nm range. Using a 532 ± 2nm narrow band pass optical filter, most of the fluoresced light at the surface is filtered out. One of the common methods of applying Rhodamine 6G to a surface is to dope acrylic paint with ethanol and mix Rhodamine 6G. We found that clear acrylic nail polish mixed with Rhodamine 6G provided a suitable replacement. The airfoil is painted only along the illuminated plane.

The PIV data analysis in this work were done using PIVLab [14] which is an open-source MATLab based 2D PIV software. The image undergoes Contrast Limited Adaptive Histogram Equalization (CLAHE). CLAHE ensures that all regions of the image use the full bit width (this means dark regions are upscaled to use full bit width). This allows for more range between low and high contrast areas in a single image[14]. This increases the amount of valid vectors detected by 4.7 ± 3.2% [15].

Direct Fourier Transform was used with four window passes. The first pass was 128 × 128, the second pass was 64 × 64, the third pass 32 × 32, and the fourth pass 16 × 16. All passes were performed with a 50% overlap. The choice of four passes was to decrease losses of information due to particle displacement errors [14]. The PIV frames were all taken with a 20 microsecond delay between images. For each angle of attack 1000 frames are used. Turbulence intensity in the freestream reaches within 10% of the expectation value by at least 300 frames for all angles of attack.

C. Mechanical Design of the Experimetal Setup and Pitch Synchronization

The work here uses a sinusoidal motion defined by equation 1. Where k is the reduced frequency of $\pi/16$, α_0 is 4°, and α_1 is 7°. The Reynolds number is 200,000. The signal for the actuator is 16 kilo-Volt peak-to-peak. The signal frequencies considered are 3,000 Hz (St_f = 10), 8000 Hz (St_f = 26.6) 15,000 Hz (St_f = 50). The wing is pitched 10 times prior to taking any PIV frames to avoid transients due to the initial pitching motion.

$$\alpha = \alpha_0 + \alpha_1(1 - cos(2kt*)) = \alpha_0 + \alpha_1(1 - cos(2\pi f t)) \tag{1}$$

To take images at the correct timing an Arduino Due synced to the pulsed laser. A detailed description of how the entire system is synchronized can be found in Lilley et al. [10]. The algorithm which determines the movement of the airfoil checks its current position and compares it to the desired position which is a function of time (1). If the algorithm finds that moving a step clockwise or counter-clockwise moves the current position closer to the desired position, a step is taken in the corresponding direction. This method of controlling the movement pairs well with the Arduino Due's 84 MHz clock rate. Controlling the position via the velocity as opposed to position directly is not a viable approach due to the fact that the only variable which can be controlled during the operation of the stepper motor is the time between steps. When controlling the motor from a velocity perspective, for velocities near zero, the time between steps must be extremely large. This yields non-physical motion with long pauses at the zero velocity point.

D. Accuracy and Precision of the Pitching Motion

One of the concerns with rapid pitching is the accuracy and precision of the motion. In order to determine the accuracy and precision, a Phantom v7.3 high-speed camera is used to film the motion of the airfoil. MatLAB is used for computer vision toolbox to find reference points on the airfoil and calculate the angle of attack.

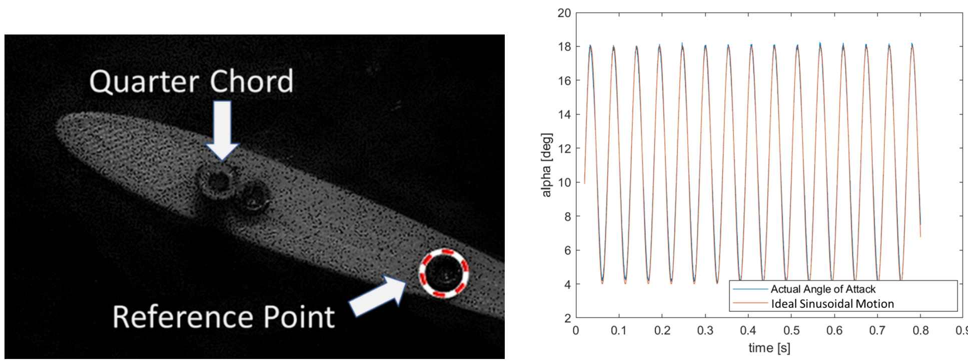

Fig. 4 Depiction of how computer vision is used to find the angle of attack of the air foil

It is of interest to quantify the error in $\alpha = 18°$ as this is the largest source of error (see Fig. 4). From review of the high-speed footage, the circle-finding algorithm has some noise. By noise, it is meant that erroneous movement of the detected reference points is seen (see Fig. 4). From the computer vision results there appears to be a max overshoot of 0.2° and undershoot of similar magnitude (see Fig. 4). Manually measuring the pixel value at the center of the reference point in Fig. 4 for every $\alpha = 18°$ yields an angle of attack of 17.98°. When using the PIV single frame cameras, measuring 50 PIV frames by pixel value at angle of attack of 18° averages 18.06°. Knowing the overshoot 0.2° is completely attributed to the circle finding algorithm, the maximum difference is 18.02 ± 0.04°.

Another source of error is frequency shift. The frequency of the wing pitching does not perfectly align with the laser. Therefore the laser frequency is shifted slightly to align with the frequency of the airfoil (The wing is pitched at 18.75 Hz, and the PIV data is collected at 6.2498 Hz vs 6.25 Hz). From the high-speed footage, the airfoil pitches at 18.75 Hz, meaning the PIV collection system, has some timing error. From the PIV images, within a single collection of 175 images, the first and last images +0.05° apart based on pixel values at $\alpha = 18$. This yields a precision 0.05°.

With the prior observations in mind, it is possible that at $\alpha = 18°$, the angle can be a maximum of 18.11° and a minimum of 18.02°.

IV. Results and Discussion

The first set of results compare baseline (counter-flow actuator off) and high frequency case (counter-flow actuator on, $\mathrm{St}_f = 50$) in Section IV.A. Next, the effect of frequency observed across various Strouhal numbers (see Section IV.B). To understand the effect of the forcing orientation, the co-flow and counter-flow actuators are compared for the higher frequency case (see Section IV.C).

A. Effect of higher frequency forcing against baseline case

Presented here are the results of the counter-flow case for the higher frequency case ($\mathrm{St}_f = 50$) in comparison to the baseline case (counter-flow actuator off case).

The baseline cases demonstrates standard dynamic stall behavior. The dynamic stall vortex can be seen forming at $\alpha = 18°$ and is apparent at $\alpha = 17°$, $\alpha = 16°$ during down-stroke (see Fig. 5). Despite the vorticity magnitude decrease from 17° down-stroke to 16° down-stroke, the vorticity near the trailing edge increases showing that the dynamic stall vortex has convected down the chord length (see Fig. 5).

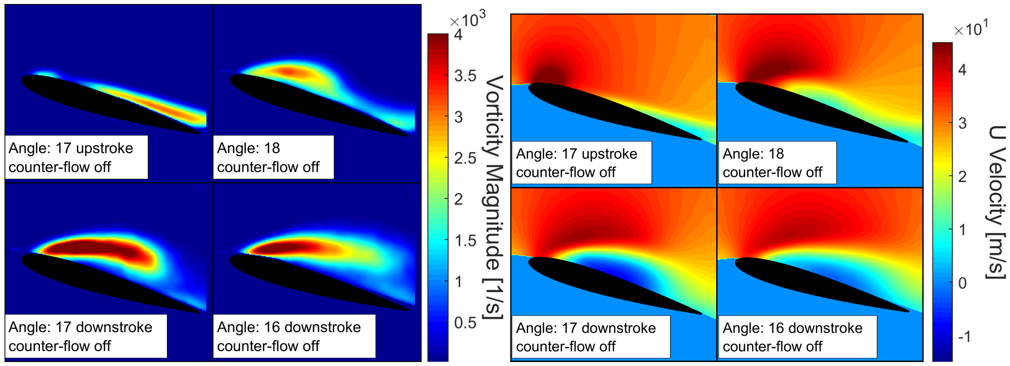

Fig. 5 Baseline case, counter-flow actuator off case. Vorticity magnitude (left) and U-velocity (right) plots

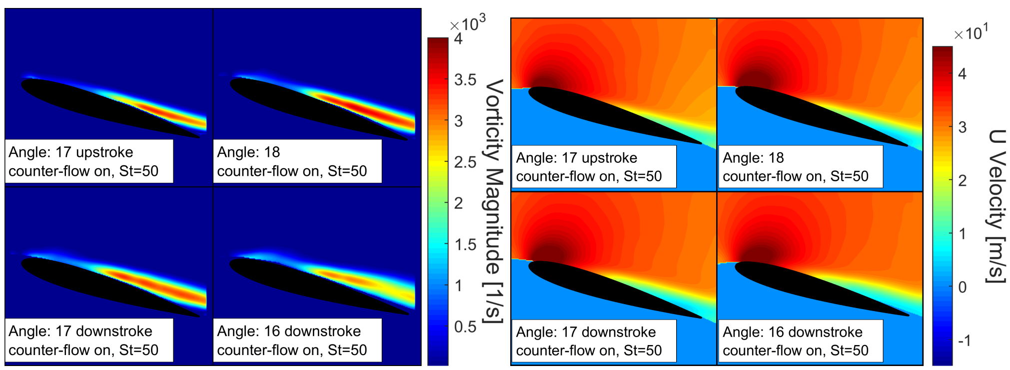

Fig. 6 Counter-flow actuator on, $\mathrm{St}_f = 50$ case. Vorticity magnitude (left) and U-velocity (right) plots

The baseline case has suction side flow reversal which is expected from dynamic stall. The flow reversal can be seen near the suction surface for the actuator off case (see Fig. 5). Although it cannot be measured, there is surely pressure differential loss across the airfoil. Velocity extractions at different points along the chord length show velocity profiles which resemble boundary layers with an adverse pressure gradient meaning stalled flow (see Figs. 8a, 9a, 10a). As the airfoil for the baseline case pitches downward, the velocity near the trailing edge (x/c=0.09) continues to remain depressed, showing that the dynamic stall process has not ended (see Figs. 9a, 10a). Similarly at x/c=0.05 it can be seen (in Figs. 8, 9a, 10a) that flow near the suction-side reverses further from 18° to 16°.. The velocity profiles reveal that the flow is completely separated at x/c=0.05 for the entire down-stroke. Streamline plots show recirculation regions for the down-stroke at $\alpha = 17°$ and $\alpha = 16°$ (see Fig. 7).

The actuator on, $\mathrm{St}_f = 50$ case is characterized by attached flow. As seen in Fig. 6, the trailing edge of the high frequency case shows a velocity gradient normal to the suction side surface at every angle of attack. Inflection of the velocity profiles can be seen across various angles of attack near the trailing edge (see Figs. 8b,9b,10b). Despite the inflection of the near trailing edge velocity profiles, the streamline plots indicate the flow remains largely conformal to the suction side surface (see Fig. 7).

From Fig. 6, the high frequency case shows no flow reversal, indicating no separation throughout the peak angle of attack (18°) and the down-stroke (17° and 16°). On the contrary, the actuator off case suffers from flow reversal at x/c=0.05 for 18°, 17° down-stroke, and 16°.

B. Effect of frequency on dynamic stall delay

The effect of frequency is observed by comparing actuator on $\mathrm{St}_f = 10$, $\mathrm{St}_f = 26.6$, and $\mathrm{St}_f = 50$. It can be seen that during the up-stroke at $\alpha = 17°$ the trailing edge shows an attached high velocity gradient region for all actuator on cases (see Figs. 11,12,6).

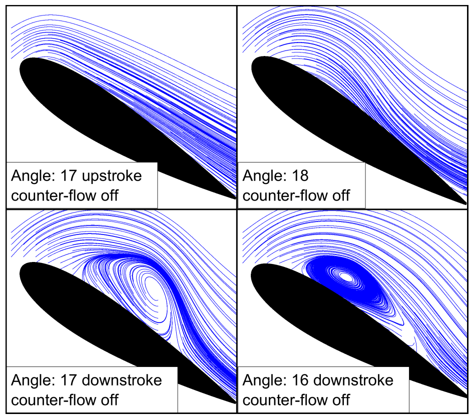

(a) Baseline case (actuator off)

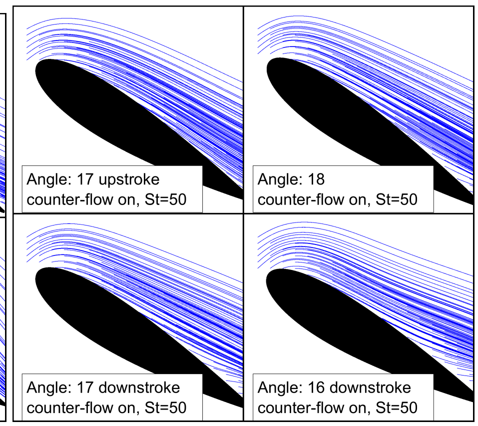

(b) St$_f$ = 50 (actuator on)

Fig. 7 Streamline plots for $17°$ up-stroke, $18°$, $17°$ down-stroke, and $16°$ down-stroke. The vertical axis is enlarged to show detail.

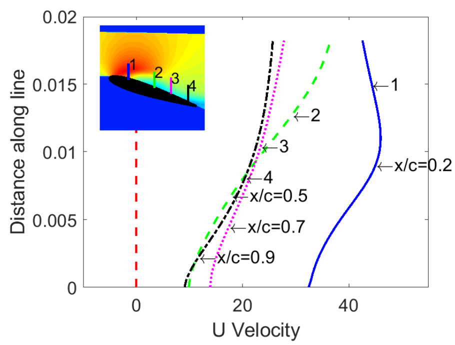

(a) Actuator off $\alpha = 18°$, velocity extraction at x/c=0.2, 0.5, 0.7, and 0.9

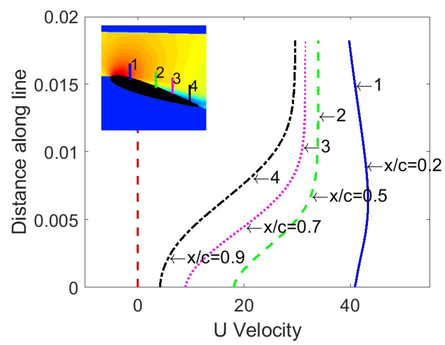

(b) Actuator on St$_f$ = 50, $\alpha = 18°$, velocity extraction at x/c=0.2, 0.5, 0.7, and 0.9

Fig. 8 Velocity extractions along chord length for actuator off and actuator on St$_f$ = 50 at $18°$ angle of attack.

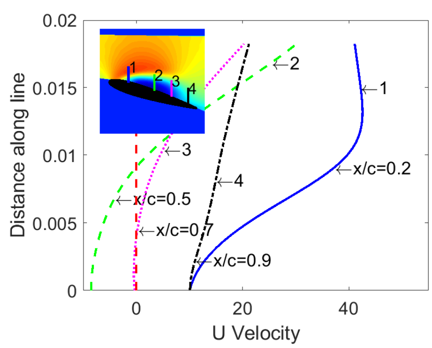

(a) Actuator off $\alpha = 17°$ during the down-stroke, velocity extraction at x/c=0.2, 0.5, 0.7, and 0.9

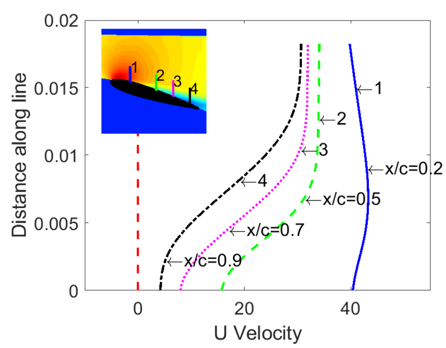

(b) Actuator on St$_f$ = 50, $\alpha = 17°$ during the down-stroke, velocity extraction at x/c=0.2, 0.5, 0.7, and 0.9

Fig. 9 Velocity extractions along chord length for actuator off and actuator on St$_f$ = 50 at $17°$ angle of attack during the down-stroke.

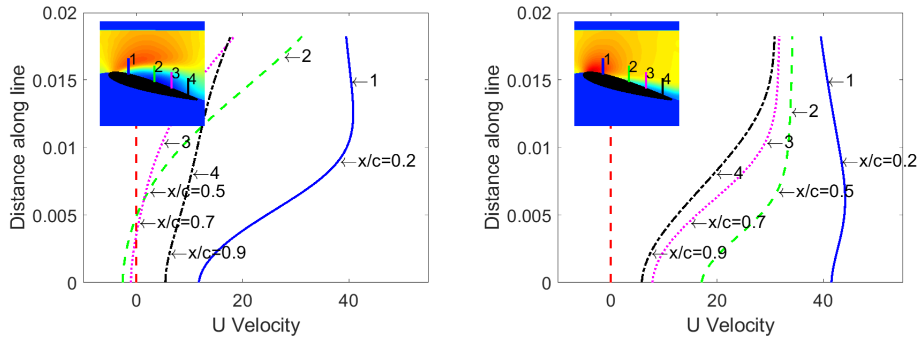

(a) Actuator off $\alpha = 16°$ during the down-stroke, velocity extraction at x/c=0.2, 0.5, 0.7, and 0.9

(b) Actuator on $\mathrm{St}_f = 50$, $\alpha = 16°$ during the down-stroke, velocity extraction at x/c=0.2, 0.5, 0.7, and 0.9

Fig. 10 Velocity extractions along chord length for actuator off and actuator on $\mathrm{St}_f = 50$ at $16°$ angle of attack during the down-stroke.

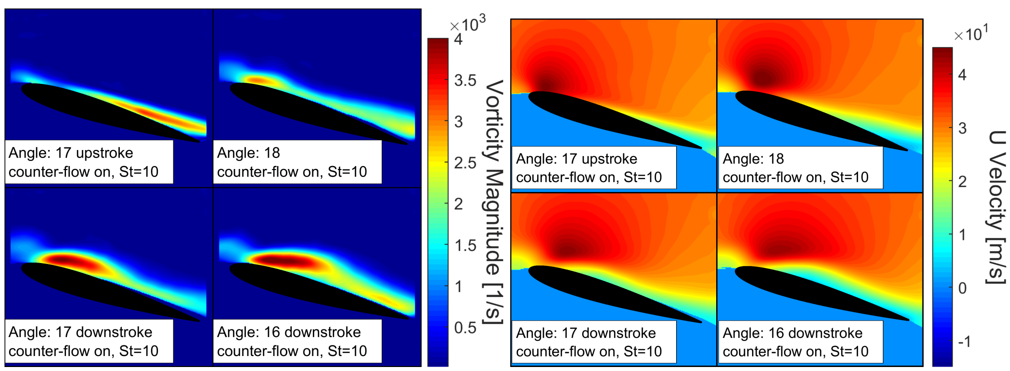

Fig. 11 Counter-flow actuator on, $\mathrm{St}_f = 10$ case. Vorticity magnitude (left) and U-velocity (right) plots

At $\alpha = 18°$, the actuator on cases begins to differ in an apparent manner. The trailing edge velocity gradient is decreased and thickened for $\mathrm{St}_f = 10$ at $\alpha = 18°$ indicating flow slow down (see Fig. 11). Near the leading edge the dynamic stall vortex appears to be forming for $\mathrm{St}_f = 10$ and $\mathrm{St}_f = 26.6$ cases at $\alpha = 18°$ (see Figs. 11,12). On the contrary the $\mathrm{St}_f = 50$ does not display any formation of leading edge structures and high velocity gradient at the trailing edge (see Fig. 6).

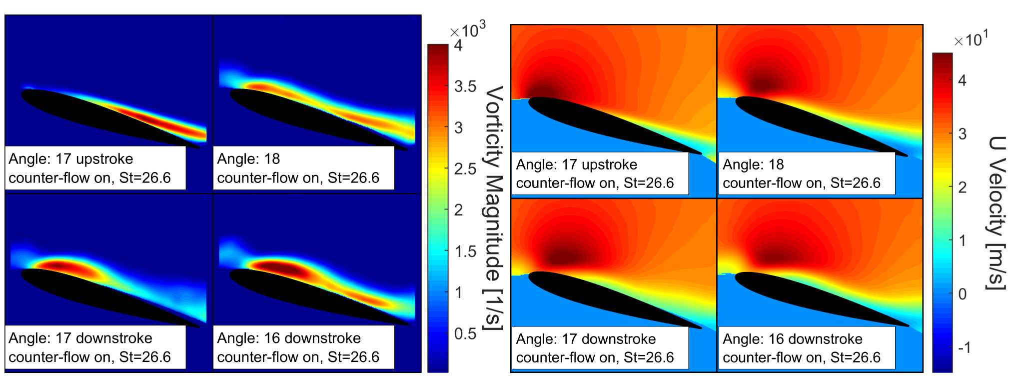

Fig. 12 Counter-flow actuator on, $\mathrm{St}_f = 26.6$ case. Vorticity magnitude (left) and U-velocity (right) plots

During the down-stroke at $\alpha = 17°$, the trailing velocity gradient decreases for $\mathrm{St}_f = 10$ and $\mathrm{St}_f = 26.6$, while the

$\mathrm{St}_f = 50$ case maintains a high velocity gradient (see Figs. 11,12,6). At $\alpha = 17°$ during the down-stroke for $\mathrm{St}_f = 10$ and $\mathrm{St}_f = 26.6$ cases, there appears to be a partially suppressed dynamic stall vortex occurring (see Figs. 11,12). During the down-stroke at $\alpha = 17°$ for $\mathrm{St}_f = 50$ case, there is no dynamic stall vortex (see Fig. 6). When comparing the U velocity at $\alpha = 17°$ during the down-stroke, the $\mathrm{St}_f = 10$ and $\mathrm{St}_f = 26.6$ cases have significantly lower U velocity near the mid-chord than the $\mathrm{St}_f = 50$ case (see Figs. 11,12,6). This shows an increase in stall control for the $\mathrm{St}_f = 50$ over the lower frequency cases.

At $\alpha = 16°$ during the down-stroke, the leading edge vorticity magnitude can be seen more separated from the airfoil surface for $\mathrm{St}_f = 10$ than $\mathrm{St}_f = 26.6$ (see Figs. 11, 12). For $\mathrm{St}_f = 50$ at $\alpha = 16°$, no dynamic stall vortex can be seen (see Fig. 6). Although there is no flow reversal at $\alpha = 16°$ for any of the actuator on cases, it can be seen that for $\mathrm{St}_f = 10$ and $\mathrm{St}_f = 26.6$ the flow is significantly slower than for $\mathrm{St}_f = 50$ (See Figs. 11, 12,6).

Overall, a gradient of dynamic stall control effectiveness can be seen with increasing Strouhal number (See Figs. 11, 12,6). This trend was previously supposed by Visbal [9].

C. Effect of actuator orientation

As mentioned prior, there are two possible orientations of the linear plasma actuator, co-flow and counter-flow (see Fig. 2). There are a multitude of important factors to consider here, the direction of the forcing generated, the location over which the force is applied, and the upstream disturbance due to the thickness of the exposed electrode. The co-flow case is adding momentum in the direction of the local flow on the suction side of the airfoil (see Fig. 2). The counter-flow case is adding momentum against the direction of the flow on the high pressure side of the airfoil (see Fig. 2). The exposed electrode is thickness is $70\mu m$. For the counter-flow case, the electrode functions as a forward step, while for the co-flow the electrode functions as a backward step (see Fig. 2). Here both co-flow and counter-flow actuator orientations are considered with actuator off and actuator on for the higher frequency case ($\mathrm{St}_f = 50$).

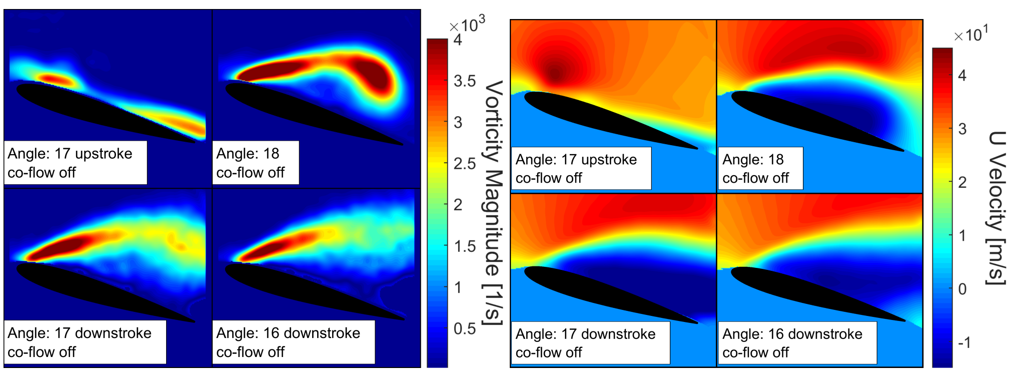

Fig. 13 Co-flow actuator off case. Vorticity magnitude (left) and U-velocity (right) plots

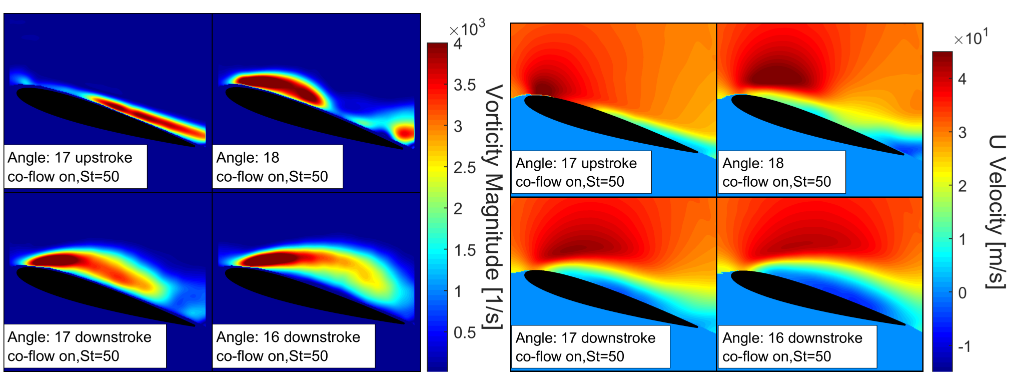

Fig. 14 Co-flow actuator on, $\mathrm{St}_f = 50$ case. Vorticity magnitude (left) and U-velocity (right) plots

The co-flow actuator off case displays strong formation of the dynamic stall vortex, by $\alpha = 18°$ the dynamic stall vortex has convected to the trailing edge (see Fig. 13). For the down-stroke, there is total separation and flow reversal (see Fig. 13). The co-flow actuator on case shows a thickened trailing edge boundary layer at $\alpha = 17°$ during the up-stroke followed by a partially suppressed dynamic stall vortex formation (see Fig. 14). Although the flow is clearly influenced by the actuator, the co-flow on case does not prevent flow reversal during the down-stroke (see Fig. 14).

When comparing the actuator off cases for both co-flow and counter-flow at $\alpha = 18°$, it can be seen that the dynamic stall vortex more strongly formed for the co-flow case (see Figs. 5,13). During the down-stroke at $\alpha = 17°$, the degree of separation for the counter-flow actuator off and co-flow actuator on is very similar, indicating that the passive disturbance introduced by the thickness of the actuator is significant (see Figs. 5,14). From $\alpha = 17°$ to $\alpha = 16°$ during the down-stroke, only the counter-flow actuator on case does not have any suction side flow reversal (see Figs 5,13,6,14). By $\alpha = 16°$ during the down-stroke, all cases, except actuator on counter-flow, display near zero velocities from the quarter chord to the trailing edge (see Figs 5,6,13,14).

V. Conclusion

Dynamic stall is prevented using plasma actuators for a NACA0012 that pitches sinusoidally between $\alpha = 4°$ and $\alpha = 18°$ (see Eq. 1). The effectiveness of plasma actuation increases with increasing Strouhal number (up to $\mathrm{St}_f = 50$ considered). The actuator off case undergoes dynamic stall which begins at $\alpha = 18°$. The dynamic stall vortex can be seen by $\alpha = 18°$ (see Figs. 5,13). As the airfoil pitches down the dynamic stall vortex can be seen moving down the chord length of the airfoil. Suction side flow reversal occurs and a large flow slow-down occurs.

For the lowest frequency considered ($\mathrm{St}_f = 10$), the actuator delayed dynamic stall although once the down-stroke began the airfoil underwent dynamic stall. The suction-side flow does not undergo flow reversal although it is slowed. Similarly, the intermediate frequency case ($\mathrm{St}_f = 26.6$) also underwent dynamic stall once the down-stroke began although with lesser trailing edge flow slow-down. The highest frequency case ($\mathrm{St}_f = 50$) did not show any signs of dynamic stall for the motion observed. The highest frequency case also maintains the highest velocity on the suction side.

The effectiveness associated with increasing frequency is most likely will yield diminishing returns. The reasoning here is based on the work of Visbal, where laminar separation bubble fluctuations at $\mathrm{St}_f = 120$ for a static NACA0012 at $\alpha = 8°$ were observed [9]. Visbal used square forcing at $\mathrm{St}_f = 50$ for a dynamic stall case to force higher harmonics and saw a delay in suction collapse of 7°[9]. Therefore it is expected that diminishing returns would be seen as the Strouhal number increases to the frequency of $\mathrm{St}_f = 120$. Future work should center around this range of forcing, although this may not be of practical use due to how high of a frequency (Hz) is required to achieve $\mathrm{St}_f > 100$.

Prior work [7][8][11][12] generally uses an amplitude modulation signal. This is where a higher frequency (5kHz) is modulated with a lower frequency (50Hz) where the lower frequency is chosen such that $\mathrm{St}_f = 1$. The work here avoids the need to modulate the signal and instead uses a single high frequency (St_f >= 10, Hz>3000) to modify the flow.

The orientation of the actuator plays a significant role in the delay of dynamic stall. By choosing a counter-flow configuration, the 70 μm exposed electrode causes a significant dynamic stall delay that can be achieved without turning on the actuator. By turning on the actuator dynamic stall is completely avoided. From the results, the flow is highly sensitive to leading edge disturbances. The counter-flow actuator passively disturbs the flow near the leading edge. When turned on the counter-flow actuator produces forcing up-stream of the laminar separation bubble (LSB), allowing for perturbations to grow before reaching the LSB. On the contrary the co-flow actuator has a backwards step at the leading edge and forces toward the suction side (near the LSB), where the perturbations have less time to grow before reaching the LSB therefore having less effectiveness.

It is important to note that this delay in dynamic stall is not through a raw momentum injection as seen by the counter-flow and co-flow comparison. In fact, the counter-flow case, which is most effective in delaying dynamic stall, the momentum addition locally opposes the flow, while the co-flow case, the momentum addition locally aligns with the flow.

Acknowledgments

This work was partially supported by the AFRL funding through OAI-C2644-19296. The authors gratefully acknowledge the help provided by the APRG members to build the wind tunnel for experiments reported in this paper. The first author would like to thank to the Graduate Student Preeminence Award (GSPA) at the University of Florida and the Student Stem Employment Program (SSEP) under the United States Air Force for funding support.

References

[1] Carr, L. W., "Progress in analysis and prediction of dynamic stall," *Journal of aircraft*, Vol. 25, No. 1, 1988, pp. 6–17.

[2] Carr, L., and McCroskey, W., "A review of recent advances in computational and experimental analysis of dynamic stall," *Fluid Dynamics of High Angle of Attack*, 1993, pp. 3–33.

[3] Corke, T. C., and Thomas, F. O., "Dynamic stall in pitching airfoils: aerodynamic damping and compressibility effects," *Annual Review of Fluid Mechanics*, Vol. 47, 2015, pp. 479–505.

[4] Carr, L., and McAlister, K., *The effect of a leading-edge slat on the dynamic stall of an oscillating airfoil*, 1983. https://doi.org/10.2514/6.1983-2533.

[5] Heine, B., Mulleners, K., Joubert, G., and Raffel, M., "Dynamic Stall Control by Passive Disturbance Generators," *AIAA Journal*, Vol. 51, No. 9, 2013.

[6] Lilley, A. J., Roy, S., Michels, L., and Roy, S., "Performance recovery of plasma actuators in wet conditions," *Journal of Physics D: Applied Physics*, Vol. 55, No. 15, 2022, p. 155201.

[7] Post, M. L., and Corke, T. C., "Separation Control Using Plasma Actuators: Dynamic Stall Vortex Control on Oscillating Airfoil," *AIAA Journal*, Vol. 44, No. 12, 2006, pp. 3125–3135. https://doi.org/10.2514/1.22716.

[8] Lombardi, A. J., Bowles, P. O., and Corke, T. C., "Closed-Loop Dynamic Stall Control Using a Plasma Actuator," *AIAA Journal*, Vol. 51, No. 5, 2013, pp. 1130–1141. https://doi.org/10.2514/1.J051988.

[9] Visbal, M. R., "Numerical Exploration of Flow Control for Delay of Dynamic Stall on a Pitching Airfoil," *32nd AIAA Applied Aerodynamics Conference*, 2014. https://doi.org/10.2514/6.2014-2044.

[10] Lilley, A. J., Roy, S., and Visbal, M. R., "Dynamics Stall delay using High Frequency Plasma Actuation," *AIAA SCITECH 2022 Forum*, 2022, p. 2125.

[11] Corke, T. C., Bowles, P. O., He, C., and Matlis, E. H., "Sensing and control of flow separation using plasma actuators," *Philosophical Transactions of the Royal Society A: Mathematical, Physical and Engineering Sciences*, Vol. 369, No. 1940, 2011, pp. 1459–1475.

[12] Mitsuo, K., Watanabe, S., Atobe, T., Kato, H., Tanaka, M., and Uchida, T., "Lift enhancement of a pitching airfoil in dynamic stall by DBD plasma actuators," *51st AIAA Aerospace Sciences Meeting including the New Horizons Forum and Aerospace Exposition*, 2013, p. 1119.

[13] Visbal, M., and Garmann, D., "Investigation of Spanwise End Effects on Dynamic Stall of a Pitching Wing Section," *Journal of Aircraft*, Vol. 56, 2019, pp. 1–13. https://doi.org/10.2514/1.C035427.

[14] Thielicke, W., and Stamhuis, E., "PIVlab–towards user-friendly, affordable and accurate digital particle image velocimetry in MATLAB," *Journal of open research software*, Vol. 2, No. 1, 2014.

[15] Shavit, U., Lowe, R. J., and Steinbuck, J. V., "Intensity capping: a simple method to improve cross-correlation PIV results," *Experiments in Fluids*, Vol. 42, No. 2, 2007, pp. 225–240.